Article:

Belucz, B., Dikpati, M., McIntosh, S.W. et al. (2023) Magnetohydrodynamic instabilities of double magnetic bands in a shallow-water tachocline model. i. cross-equatorial interactions of bands. The Astrophysical Journal, 945 (1). 32. ISSN: 0004-637X

https://doi.org/10.3847/1538-4357/acb43b

The Astrophysical Journal, 945:32 (17pp), 2023 March 1 https://doi.org/10.3847/1538-4357/acb43b

Magnetohydrodynamic Instabilities of Double Magnetic Bands in a Shallow-water Tachocline Model. I. Cross-equatorial Interactions of Bands

Bernadett Belucz[1,2,3], Mausumi Dikpati[4], Scott W. McIntosh[4], Robert J. Leamon[5], and Robertus Erdélyi[1,2,3]
[1] Solar Physics and Space Plasma Research Center, School of Mathematics and Statistics, University of Sheffield, S3 7RH, UK; b.belucz@sheffield.ac.uk
[2] Department of Astronomy, Institute of Geography and Earth Sciences, Eötvös University, Budapest, Hungary
[3] Hungarian Solar Physics Foundation, Gyula, Hungary
[4] High Altitude Observatory, NCAR, 3080 Center Green Drive, Boulder, CO 80301, USA
[5] Department of Astronomy, University of Maryland, College Park, MD 20742, USA

Received 2022 March 29; revised 2023 January 11; accepted 2023 January 14; published 2023 March 3

Abstract

Along with a *butterfly diagram* of sunspots, combined observational studies of ephemeral active regions, X-ray and EUV bright points, plage, filaments, faculae, and prominences demonstrate a pattern, which is known as the Extended Solar Cycle. This pattern indicates that the wings of the sunspot butterfly could be extended to much higher latitudes (up to ∼60°), to an earlier time than the start of a sunspot cycle, hence yielding a strong overlap between cycles. Thus, during the ongoing cycle's activity near 30° latitude in each hemisphere, the next cycle kicks off at around 60°. By representing these epochs of overlaps by oppositely directed double magnetic bands in each hemisphere, we compute the unstable eigenmodes for MHD Rossby waves at the base of the convection zone and study how the properties of these energetically active Rossby waves change as these band pairs migrate equatorward. We find that in each hemisphere the low-latitude band interacts with the high-latitude band and drives the MHD instability as the solar activity progresses from 35°–15° latitude, which is essentially the rising phase. When the activity proceeds further equatorward from 15°, the interaction between low- and high-latitude bands weakens, and the cross-equatorial interaction between two low-latitude bands in each hemisphere starts. The eigenmodes in the latitude-longitude plane also reflect such changes in their pattern as the bend of the active cycle moves below 15° latitude.

Unified Astronomy Thesaurus concepts: Solar magnetic fields (1503); Solar activity (1475); Magnetohydrodynamics (1964); Solar rotation (1524)

1. Introduction

The coronal green line emissions (Tappin & Altrock 2013), torsional oscillation signal (Howe et al. 2011), ephemeral active regions (Harvey & Martin 1973; Wilson et al. 1988; McIntosh et al. 2014a; Martin 2018), and analysis of solar torsional oscillations (Pipin & Kosovichev 2020; Snodgrass 1987; Guerrero et al. 2016) are all mounting evidence toward indicating that the solar activity cycle shows its signature of appearance at high latitudes (at about 60°–70°) prior to the start of a new sunspot cycle (see Cliver 2014 for a detailed review). This high-latitude branch does not produce sunspots. Instead, it generates ephemeral regions, most likely because these toroidal magnetic fields of the new cycle are weak at high latitudes. It should be noted that Muñoz-Jaramillo et al. (2009) demonstrated that the mid-high latitudinal differential rotation can generate a significant toroidal field. Nandy & Choudhuri (2002) suggested that the deep meridional flow transports these weaker high latitudes into the stable tachocline region, where they may not be able to erupt and form strong sunspots. It is therefore a question of how weak these fields can be. It is certain that we do not find sunspots at high latitudes, so it is reasonable to assume that the magnetic fields of high latitudes are weaker than the toroidal fields of lower latitudes.

These observations suggest that the sunspot activity cycle is the main phase of a more extended solar cycle beginning at high latitudes, which then migrates equatorward. These high-latitude magnetic branches coexist along with the active sunspot cycle. Hence the subsurface magnetic fields of the Sun may consist of double magnetic bands, oppositely directed in each hemisphere, with a low-latitude spot-producing toroidal band and a weak high-latitude band.

The spot-producing magnetic fields that drive solar activity most likely are generated at the base of the convection zone, at/near the tachocline. The kinetic energy of fluid motions is converted to magnetic energy via hydromagnetic dynamo processes. Accurately estimating the thickness of the tachocline and the overshoot layer are key issues since they determine the strength of the magnetic field that can be stored and the process by which it is transformed. The dynamo-generated toroidal bands may emerge to the surface through the convection zone either by buoyancy (Parker 1955, 1975) or by convective instability (Guerrero & Käpylä 2011; Weber et al. 2011).

The latitudinal location of sunspots and plages, when plotted as a function of time, constitute the well-known butterfly diagram. The equatorward branches of the butterfly diagram reveal the well-known nearly periodic 11 yr sunspot cycle. As each cycle proceeds, the active cycle's sunspots appear first at near 35° latitude. Then, as the activity band moves toward the equator, the sunspots also emerge closer and closer to the equator. On the other hand, smaller-scale magnetic features, like coronal bright points (McIntosh et al. 2014b) or Ca II K networks (Chatterjee et al. 2019), emerge at high latitudes of about 60°–65° at the onset time of the new cycle. They most likely appear from opposite polarity high-latitude bands in each hemisphere. This double-band system is observed to drift

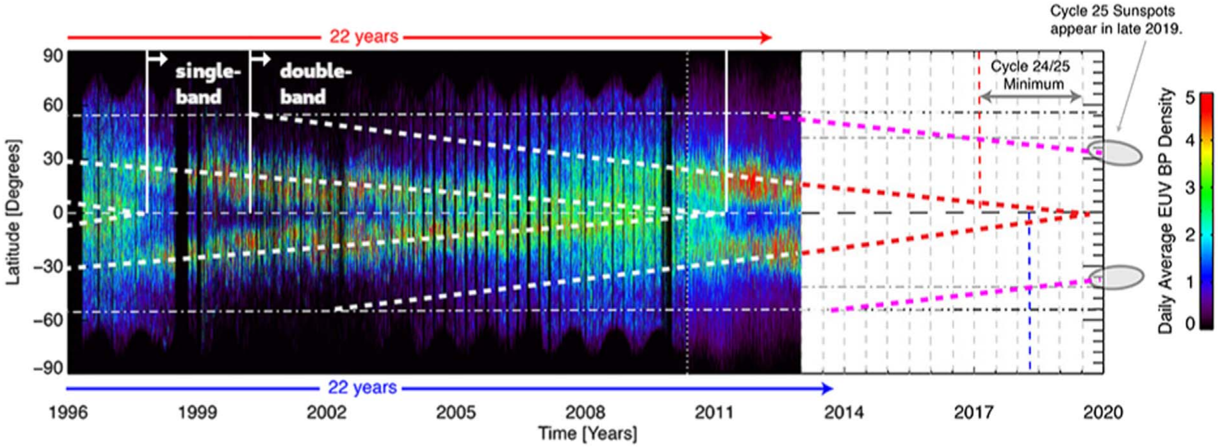

Figure 1. The extent of the magnetic activity band up to 60° based on the work in McIntosh et al. (2014b) and Chatterjee et al. (2019). The distance between the two activity bands is 30°. The double-band system is seen to exist during the late rising, peak, and declining phases.

together toward the equator as the cycle progresses (Figure 1). McIntosh et al. (2015) showed that the separation between the two bands, namely, the one representing the band producing activity and the weaker band at high latitude, the most likely representative of the next solar cycle, is about 30° in latitude. The cross-equatorial interaction across the equator, between the high-latitude and low-latitude band system in each hemisphere, gradually becomes significant.

Cally et al. (2003) demonstrated the mechanisms of interaction by studying the tipping instabilities. If the magnetic band is broad, then it opens up into a clamshell-like pattern. However, if it is narrow, it tips either in phase or antiphase, depending on whether the dominant mode is symmetric or antisymmetric about the equator. In the antisymmetric case, the bands in both hemispheres approach each other, thus creating a cross-interaction between them (see Figure 4 of Cally et al. 2003). In a symmetric case, the longitudinal flow will be antisymmetric, so in this case, the plasma flow drives the connection.

Over the past few decades, the extensive study of the global magnetohydrodynamics (MHD) of the solar tachocline has shown to play a key role in understanding the global dynamics of the Sun. Helioseismic measurements (Brown et al. 1989; Goode et al. 1991; Tomczyk et al. 1995) indicate that the transition between the latitudinal differential rotation of the convection zone and the rigid rotation of the radiative zone occurs in a very thin layer called the solar tachocline. The solar tachocline is also probably home to strong toroidal fields that are likely to be the source of the strong photospheric fields seen as active regions, as well as many other manifestations of magnetic activity observed at the solar surface and above (Galloway & Weiss 1981).

We study the global HD/MHD instabilities in the solar tachocline to understand the global MHD processes in the shear layer and their contribution to properties of solar activity and the solar cycle. Instability can arise because energy is stored in the latitudinal and radial gradients of the rotation, as well as in the latitudinal and radial gradients of the toroidal field. We focus here on the latitudinal differential rotation and analyze the MHD instability of this differential rotation and coexisting spot-producing magnetic fields, for the perturbations with low longitudinal wavenumbers ($m = 1, 2, 3, 4$). The Rossby waves, in the tachocline, work as perturbations to the system of differential rotation and toroidal magnetic fields. Here, we study this system using an MHD shallow-water model of the solar tachocline (Dikpati et al. 2018; Dikpati et al. 2021).

Numerous shallow-water models have been developed over the last few decades to model and study ocean tides and waves (e.g., Osborne et al. 1991), atmospheric zonal flows, and the connections among ocean, land, and atmosphere (e.g., Lau & Peng 1987). Gilman (2000) developed an MHD generalization of the shallow-water equations of geophysical fluid dynamics to describe the global dynamics of the solar tachocline (Gilman & Fox 1997; Cally 2001; Gilman & Dikpati 2000; Dikpati & Gilman 2001a; Schecter et al. 2001; Gilman & Dikpati 2002; Dikpati et al. 2003; Zaqarashvili et al. 2010) to analyze instabilities for a wide range of amplitudes of solar latitudinal differential rotation and the toroidal field below the base of the convection zone. The global MHD shallow-water instability of differential rotation and toroidal field bands provides a possible mechanism for the formation and evolution of active longitudes (Dikpati & Gilman 2005). Dikpati et al. (2017) showed that the form of quasi-periodic bursts of activity can be explained as being due to tachocline nonlinear oscillations.

Our goals in this paper are to study the global MHD instabilities of a double-band system in the tachocline, using a shallow-water model. For this, the profile representing a double-band system is mathematically prescribed by Gaussian functions (see, e.g., Dikpati et al. 2018). The observations (see, e.g., Figure 1) indicate that the separation between the two bands in each hemisphere can be about 30°; so, in this paper, we focus on a band separation of 30° in each hemisphere. We will also limit our study to a bandwidth of 10° in latitude. We explore in detail the features of the instability as the double-band system in each hemisphere migrates toward the equator, as they do with the progression of the solar cycle. Our main aim is to study when the double-band systems in each hemisphere start cross-equatorial interaction with their opposite-hemisphere counterparts. We also explore the variation in peak field strength of the low-latitude and high-latitude bands. The next section describes the mathematical formulations, we present our results in Section 3, and conclude in Section 4.

2. Mathematical Formulation

2.1. Nonlinear MHD Shallow-water Equations

Formulation of a nonlinear shallow-water system, applied to the solar tachocline, has been extensively presented in various

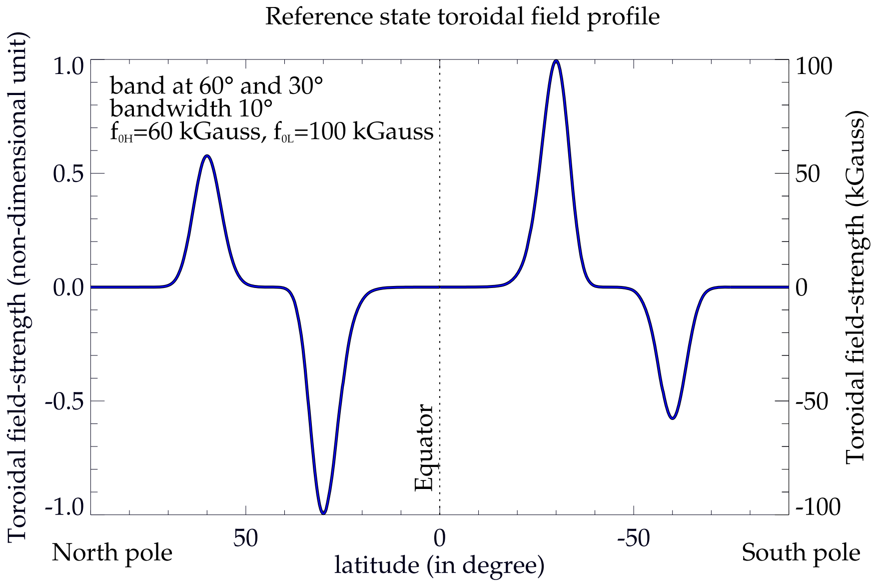

Figure 2. Reference state toroidal field profiles for four different locations. The bandwidths are 10°, and the peak field strength of the low-latitude band is 60 and 100 kG at the high-latitude band, respectively.

papers, such as Gilman (2000), who built the MHD shallow-water model in vector-invariant form. Later, the models were employed in spherical geometry (see, e.g., Zaqarashvili et al. 2009; Dikpati et al. 2018; Zaqarashvili 2018). These papers contain the details of the basic physics for building a shallow-water model, including a full set of nonlinear MHD shallow-water equations. Here, we briefly discuss the shallow-water system, and provide the details of the equations in a rotating frame of reference in Appendix A and B.

Given its thin nature, the solar tachocline can be modeled in a shallow-water formalism, which presents a thin fluid shell with a rigid bottom and deformable top surface. The velocities, magnetic fields, and perturbations to the system are much larger in the horizontal (i.e., latitude and longitude) than in the vertical (radial) direction. These conditions are fulfilled in the tachocline plasma fluid because of its location in a subadiabatic region in the interior of the Sun. Details of the formalism and the development of the model as well as the equations can be found in earlier papers, such as in Dikpati et al. (2018).

Let us define the velocity as $\boldsymbol{V} = u\hat{\lambda} + v\hat{\phi}$ and the magnetic field as $\boldsymbol{B} = a\hat{\lambda} + b\hat{\phi}$, where $\hat{\lambda}$ and $\hat{\phi}$ are unit vectors in the longitudinal and latitudinal directions. The horizontal flows are independent of height (i.e., the radial direction), while the radial velocity (w) is a linear function of height. The equations are made nondimensional by using the radius (r_0) of the shell as the unit length and the inverse of the interior rotation rate (ω_c) as the unit of time.

The nondimensional parameter of the model is the effective gravity, G, the formulation of which is presented in detail in Appendix A and B.

The latitudinal differential rotation, as derived from helioseismology, can be expressed in the rotating frame as

$$\omega_0 = s_0 - s_2\mu^2 - s_4\mu^4 - \omega_c, \tag{1}$$

where μ is the sine latitude and s_0, s_2, s_4 are coefficients. The interior rotation rate, (ω_c) approximately matches the rotation rate at 32° latitude at the tachocline. The s_0 parameter is the rotation rate at the equator and the differential rotation amplitude becomes $(s_2 + s_4)/s_0$ (Dikpati et al. 2018).

The latitudinal profile of the band can be prescribed in various ways, but we follow Dikpati & Gilman (1999) using the same prescription given by a Gaussian function previously used by others (Cally 2001; Cally et al. 2003) to represent the high-latitude and low-latitude, spot-producing toroidal magnetic bands. The toroidal magnetic bands of the reference state ($a_0 = \alpha_0 \cos\phi$; α_0 is the angular measure) are expressed as

$$\begin{aligned}\alpha_0 = {} & p_h f_{0h}\,(e^{-\beta_h(\mu-d_{sh})^2} - e^{-\beta_h(\mu+d_{sh})^2})\\ & + p_l f_{0l}\,(e^{-\beta_l(\mu-d_{sl})^2} - e^{-\beta_l(\mu+d_{sl})^2}).\end{aligned} \tag{2}$$

In expression (2), f_{0n} ($n = h$, l shows the parameters of the high-latitude and low-latitude bands) is the field strength ($f_{0n} = 0.1$ is 10 kG in real units), β_n controls the width of the toroidal field band, d_{sn} is the sine latitude of the center of the band, and p_n are the prefactors to scale the peak field strength with the change in β_n in the Gaussian profile, so that the value of f_{0n} denotes the peak field strength . The width of the toroidal field band is $2\beta_n^{-1/2}$, which is the normal FWHM for a Gaussian profile. This width represents the width in μ; therefore, the actual latitudinal width of the toroidal field band is given by $\delta\phi_n = 2(\beta'_n)^{-1/2}$, where β'_n is $\beta_n(1 - \mathrm{d}_{sn}^2)$. Figure 2 shows the toroidal field profiles for different locations of bands.

3. Results

We present our results in three subsections. It could be instructive if we first show the results of MHD instability for a fixed active cycle's band (i.e., the low-latitude band), while the high-latitude band's peak field strength varies. This setup is designed to help us understand the role of a high-latitude band in driving this instability. Section 3.1 below is devoted to this exploration.

In Section 3.2, we present the results of the detailed parameter space survey, namely, varying the field strength of both the low- and high-latitude bands, and making the band system migrate toward the equator, but keeping the separation between the low- and high-latitude band centers at 30°. While in this paper we study the properties of unstable modes only for

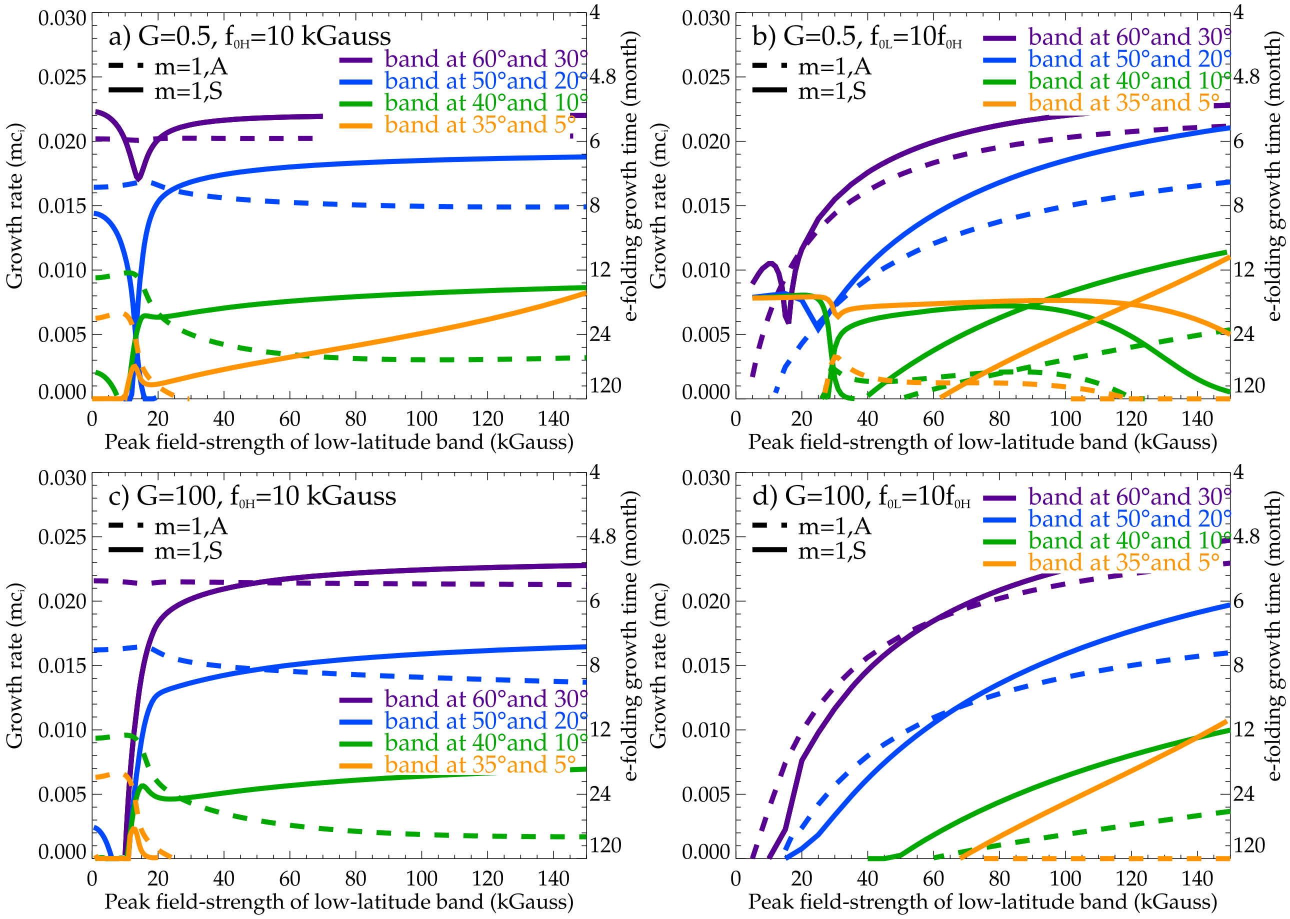

Figure 3. Growth rates of unstable modes with longitudinal wavenumber $m = 1$ are displayed, respectively, in the top (an overshoot tachocline with effective gravity $G = 0.5$) and bottom panels (a radiative tachocline with effective gravity $G = 100$) also. Panels (a) and (c) display growth rates as a function of the peak field strength of the low-latitude toroidal band. The peak field strength of the high-latitude toroidal band is kept fixed at 10 kG. The double toroidal bands are placed at different latitudes. Panels (b) and (d) display growth rates for a double-band system as a function of the field peak strength of both bands, whereas the ratio of field strengths is kept fixed. Solid lines denote growth rates for symmetric modes, and the dashed lines denote the antisymmetric modes.

30° separation between the low- and high-latitude bands, we explore both the high and low effective gravity values, respectively, for $G = 100$ and 0.5. A future paper will report the results for different separations, namely, for 25° and 35° latitude separations between the bands in each hemisphere. In Section 3.3, we show the structure of eigenfunctions in the latitude-longitude plane.

3.1. Role of the High-latitude Band

Previous analyses of linear and nonlinear unstable global MHD modes were performed by using a single toroidal band profile (Dikpati et al. 2003). As discussed in Section 1, our present study is motivated by observations of the extended solar cycle, which is representative of oppositely directed double toroidal bands in each hemisphere. The high-latitude branch coexists along with the low-latitude spot-producing toroidal bands of the active cycle. The disturbance growth rates (mc_i) and phase speeds of the linear unstable MHD modes, which are essentially the Rossby wave modes, have been estimated for a band pair of 10° latitudinal width. The profile of the toroidal field is represented by a double Gaussian function, see, e.g., Equation (2). We analyze linear modes of both symmetries about the equator. For the symmetric case, v and a are symmetric, u and b are antisymmetric about the equator, as long as antisymmetric modes v and a are antisymmetric, u and b are symmetric. We consider two characteristic G values, representative of the overshoot tachocline ($G = 0.5$) and the radiative tachocline ($G = 100$). In a nondimensional unit, $a = 1$ corresponds to a peak field strength of 100 kG (Gilman & Fox 1997).

One of the most important questions is whether the two bands play the same role in the instability, or whether one band is more important. If the latter is true, then which one is more important? That is why we examined whether to keep the peak strength of one or the other band. We compared the growth rates with the case when the strength of both bands changes and only the ratio is kept constant. Can we find differences that can illustrate that the role of one or the other band is more significant? In Figures 3 and 4, the left panels (i.e., panels (a) and (c)) show the results for a double-band case when the strength of one band is constant; the right panels (i.e., panels (b) and (d)) show the results for a double-band case with a fixed ratio of strength. Figures 3 and 4 show the growth rates, respectively, for $G = 0.5$ (panels (a) and (b)) and $G = 100$ (panels (c) and (d)). The peak field strength of low-latitude bands is varied from 1 to 150 kG, keeping the peak field strength of the high-latitude band fixed at 10 kG. In the opposite case, the peak field strength of the low-latitude band is fixed at 100 kG.

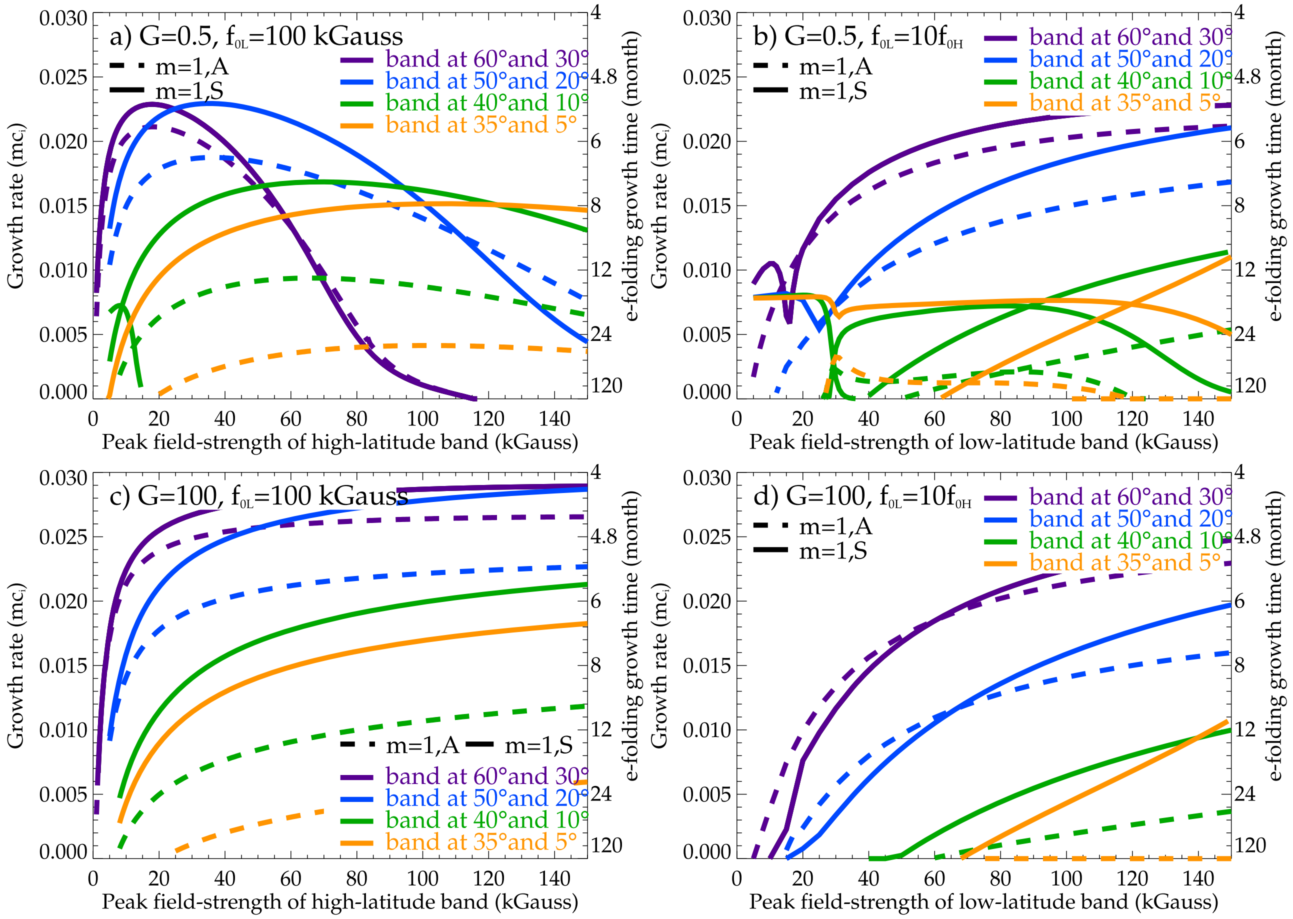

Figure 4. Same as in Figure 3, but the peak field strength of the low-latitude toroidal band is kept fixed at 100 kG in panels (a) and (c).

Figures 3 and 4 immediately reveal several important features. First, the modes with longitudinal wavenumber $m = 1$ are greatly unstable for both G values. For the single-band case, such results have already been obtained previously (Dikpati et al. 2003). Second, a double-band system produces similar growth rates except when a single band is at a very low latitude (lower than 20° or so). However, the presence of a high-latitude band in such cases makes the band system significantly unstable. Essentially the high-latitude band, whether single or having an oppositely directed low-latitude part, primarily drives the instability.

Another feature that can be seen by comparing the top panels of Figure 3 with those of Figure 4 is that the $m = 1$ modes vanish for a large enough field strength for $G = 0.5$, but for $G = 100$ they reach asymptote as the field strength increases. For $G = 100$ the radial motions are much less, and hence these modes behave very much like the 2D case. Such asymptotic behavior of $m = 1$ modes was found in 2D by Cally et al. (2003) for single-band cases. This feature can also be seen in a double-band system in the case of high G.

In this subsection we showed, using a few examples, the characteristic features of how the presence of a high-latitude band in a double-band system produces changes in the instability pattern. We fixed the field strength of the low-latitude band at 10 kG and varied the field strength of the high-latitude band from 1 to 150 kG. We found that in all cases the instability is primarily driven by the high-latitude band.

Note that, for a band of 10° latitudinal width, the peak of the low-latitude band of a double-band system can migrate to the lowest of 5° latitude, below which the low-latitude band would annihilate its opposite-hemisphere counterpart. For a double-band system, the high-latitude band can be as low as 35° latitude only. The question is if the low-latitude band is strong enough, can it still not be the primary driver of the instability? Obviously to find the answer to this question, we need to explore the detailed parameter space in the field strengths of the two bands. The next section presents the detailed calculations.

3.2. Double-band Migrations and Changes in Features

We performed a detailed survey of growth rates of $m = 1$ unstable modes for both symmetries. We show in Figures 5 and 6, respectively, for $G = 0.5$ and 100, the contours of growth rates as the band system migrates equatorward from top to the bottom, namely, from 60°–30° (aa), (ab) through 50°–20° (ba), (bb), and 40°–10° (ca), (cb) down to 35°–5° (da), (db). Note that the first latitude indicates the location of the high-latitude band and the second one the low-latitude band; for example, 60°–30° in (aa), (ab) denotes that the high-latitude band is at 60° latitude and the low-latitude band is at 30° latitude. In all panels, the vertical axis is for the field strength of the low-latitude band, and the horizontal axis for the high-latitude band's strength. The four frames at the left show the antisymmetric modes and at the right the symmetric modes.

(aa) bands at 60° and 30°; G=0.5; m=1,A

(ab) bands at 60° and 30°; G=0.5; m=1,S

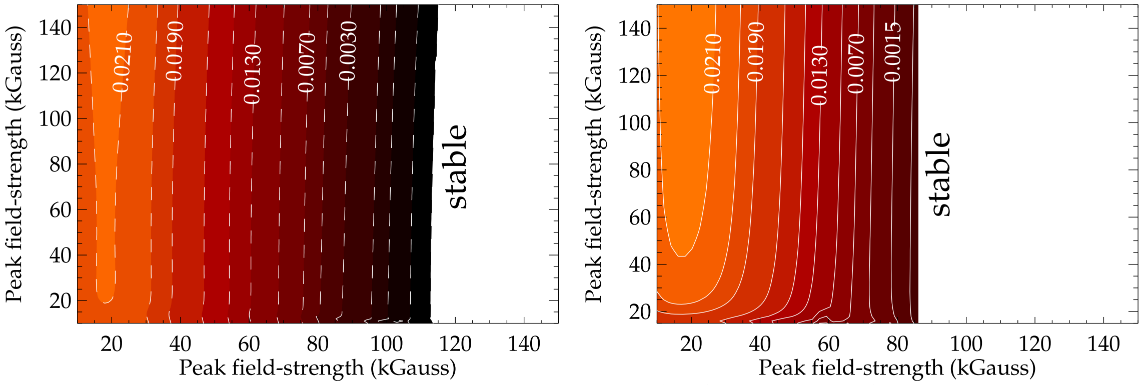

(ba) bands at 50° and 20°; G=0.5; m=1,A

(bb) bands at 50° and 20°; G=0.5; m=1,S

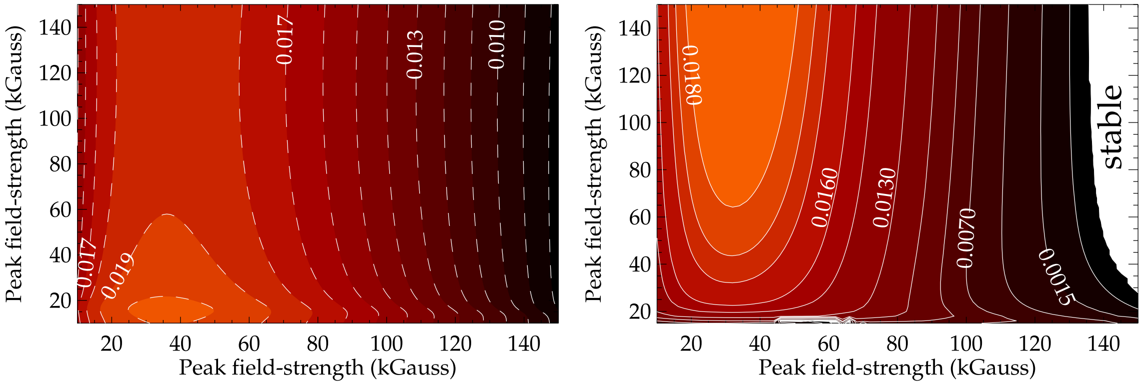

(ca) bands at 40° and 10°; G=0.5; m=1,A

(cb) bands at 40° and 10°; G=0.5; m=1,S

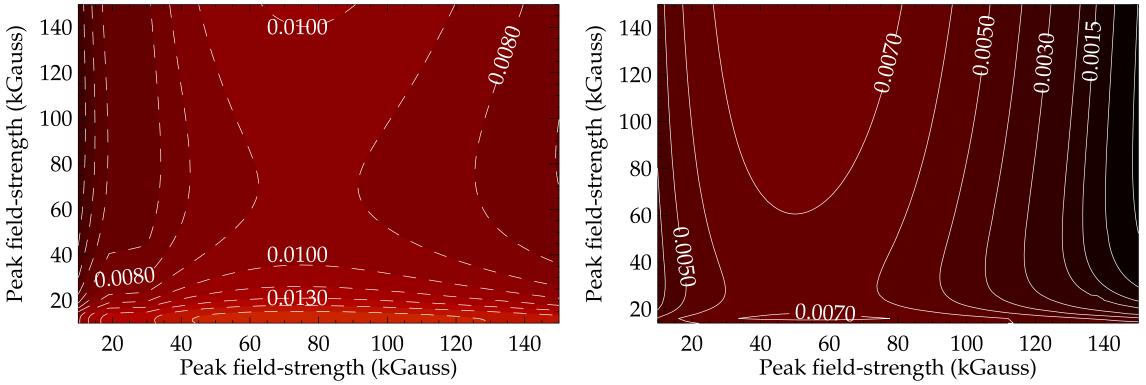

(da) bands at 35° and 5°; G=0.5; m=1,A

(db) bands at 35° and 5°; G=0.5; m=1,S

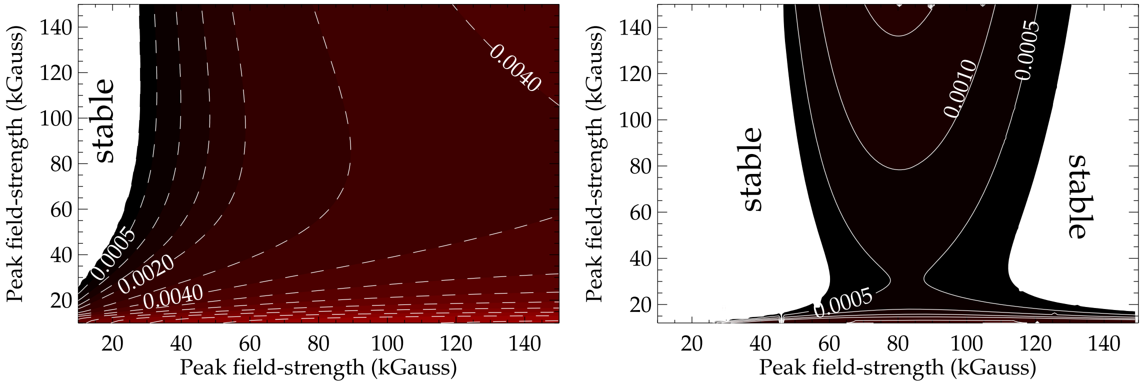

Figure 5. For $G = 0.5$, growth rate contours for $m = 1$ modes are displayed in the field strength space, in which the x-axis denotes the strength of the high-latitude band and the y-axis that of the low-latitude band. The left and right panels represent, respectively, the antisymmetric ($m = 1$, A) and symmetric ($m = 1$, S) modes. As the band system migrates from high latitudes toward the equator, the four rows from top to bottom show how the instability features change, respectively, for bands at 60° and 30° (aa), (ab); 50° and 20° (ba), (bb); 40° and 10° (ca), (cb); and 35° and 5° (da), (db).

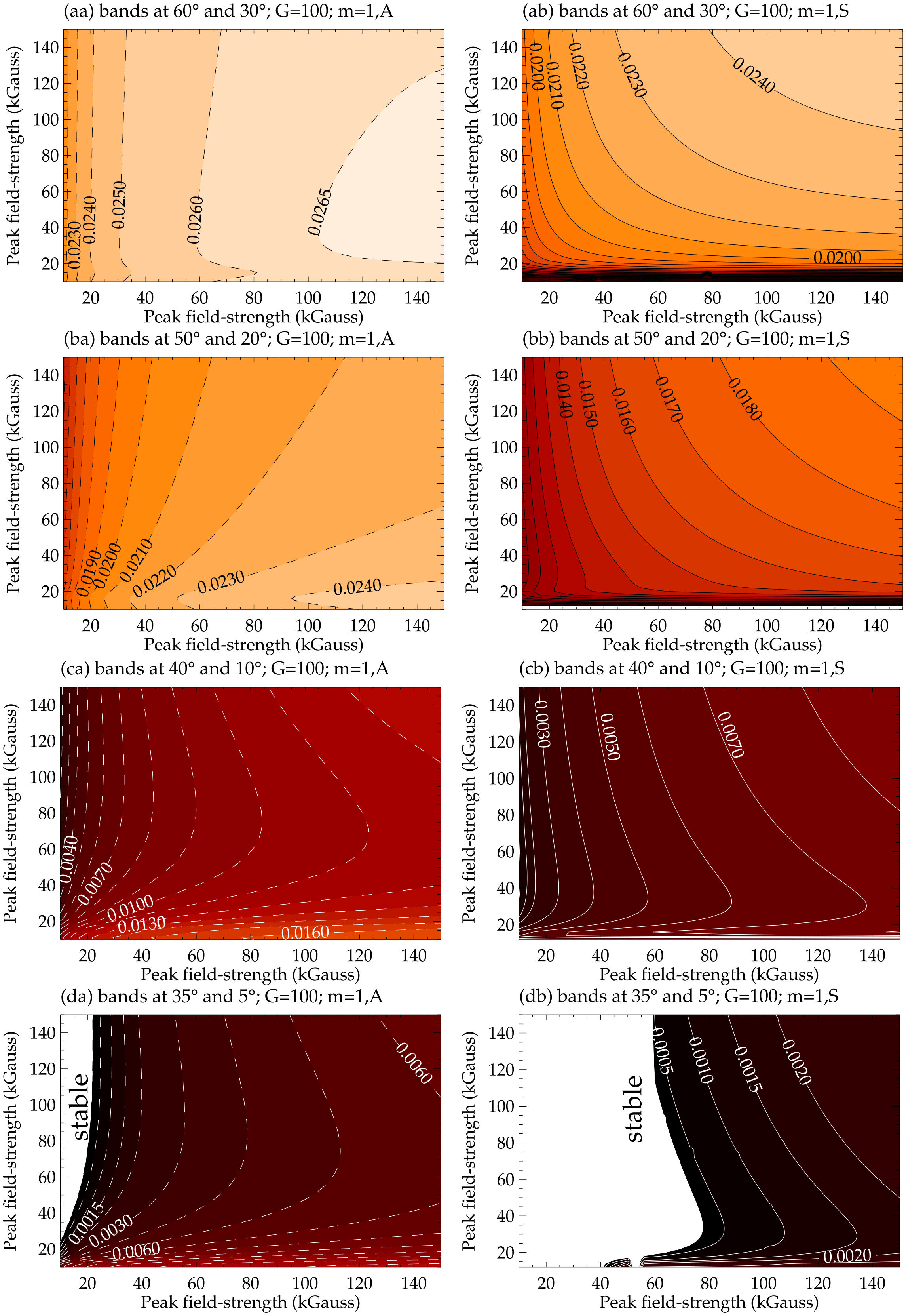

Figure 6. The same as in Figure 5, but for $G = 100$.

Figure 5 reveals many interesting features of the instability of a double-band system. First, the antisymmetric and symmetric modes show similar features when the band system is at latitudes sufficiently far away from the equator, namely, the high- and low-latitude bands at 60° and 30° latitudes, respectively (see the top panels (aa) and (ab)). Note that the lighter color denotes higher growth rates in this red-hot color map, and the darkest color the slowest growth rates. In both cases, it is clear that the high-latitude band is the primary driver of the instability, whereas the low-latitude band is responsible for the interaction between the bands. The lighter vertical region implies that the largest growth rates occur for weaker high-latitude bands with a peak field strength of about 20 kG, almost irrespective of the strength of the low-latitude band at 30°. Nearly vertical contours in the top row in both frames (i.e., for both symmetries) reinforce the feature that the high-latitude band is the primary driver in this case, making the low-latitude band interact. We recall that the low-latitude band is the active cycle's band, and the high-latitude band represents the extended cycle to appear as the next cycle.

As the band system migrates toward the equator, panels (ba) and (bb) show that when the high-latitude band is at 50° and the low-latitude band at 20° latitude, the low-latitude band starts to take a more active role in driving the instability. This active role along with the high-latitude band up to a certain field strength of about 60 kG, beyond which the high-latitude band again becomes the major driver of the instability. Elliptical-type patterns of the lighter-colored contours, particularly in panel (ba) and to some extent in panel (bb) illustrate the active interactions between the high- and low-latitude bands. We also see the symmetry switching in this case, namely, the antisymmetric modes (see the dashed contours) are more unstable than the symmetric modes (solid contours) for a peak field strength of about 50 or 60 kG of the low-latitude band. However, the symmetric modes become more unstable than the antisymmetric modes when the low-latitude band becomes stronger than 60 kG.

Panels (ca) and (cb) show the growth rates of instabilities when the double-band system migrated 10° more, namely, the high- and low-latitude bands being, respectively, at 40° and 10° latitudes. In both panels lighter-colored contours spread toward the right, indicating that both the high- and low-latitude bands are interacting to drive the instability, instead of the high-latitude band being the primary driver. For the antisymmetric modes, as can be seen in panel (ca) (see, e.g., the lightest-colored contours along the horizontal axis) that the highest growing modes occur when there is a reasonably strong high-latitude band, despite the low-latitude band being as weak as 10 kG. By contrast, as can be seen in panel (cb) the situation is different for the symmetric modes; the lightest-colored contours occur for a much stronger low-latitude band of more than 110 kG field strength and a moderate high-latitude band of about 50 kG field strength. We also do not see many vertical contours except for in the darker-colored contours. Note that the low-latitude band at 10° means that the active cycle is in its declining phase.

When the double band has migrated a further 5° equatorward, namely, the high- and low-latitude bands being, respectively, at 35° and 5° latitudes, the unstable zone shrinks for both symmetries (see panels (da) and (db)). The maximum growth rates (lightest-colored contours) occur for the weak low-latitude band of less than 10 kG strength in the case of antisymmetric modes (panel (da)) and more than 140 kG in the case of symmetric modes. So for a wide range of field strengths of the low-latitude band, the system is either very weakly unstable or even stable. We know from Section 3.1 that a single band at 35° can be very unstable. However, here we can see that due to the presence of the low-latitude band at 5° latitude during the late declining phase of the active cycle, the double-band system is either stable or just weakly unstable. The low-latitude band is behaving like a barrier here for the high-latitude band, which is about to create the onset of the next cycle. The onset happens only after the annihilation of the low-latitude band with its opposite-hemisphere counterpart, plausibly through the mechanism of a tsunami-like event (see Dikpati et al. 2019 for details).

Figure 6 shows the growth rate contours for $G = 100$, which is representative of the radiative tachocline. Again, as in Figure 5, the rows from top to bottom show how the instability features change as the double-band system migrates equatorward. Panels (aa) and (ab) show oppositely directed bands at 60° and 30°, respectively. Comparing panel (aa) with panel (ab), distinctly different features can be seen for the antisymmetric and symmetric modes. For antisymmetric modes, one can see that the growth rate contours are parallel to the vertical axis, indicating that the high-latitude band is the primary driver of the instability, irrespective of the strength of the low-latitude band. The growth rate increases in this case when the strength of the high-latitude band increases. On the other hand, for the symmetric modes displayed in the right panel (see panel (ab) of Figure 6), it can be seen that both the high- and low-latitude bands participate in driving the instability. This is evident from the growth rate contours, which show an increase with the increase of both field strengths, and the highest growth rates (the lightest-colored contours) are shown in the top right corner of panel (ab).

As the band system moves toward the equator, panels (bb) and (cb) show a similar pattern for the symmetric modes (the right panels), indicating that both the high- and low-latitude bands continue to participate in driving the instability, but stronger fields are required to drive the unstable modes with the same growth rates. However, for the antisymmetric modes (see the left panels (ba) and (ca)), it can be seen that irrespective of the field strength of the low-latitude band, the high-latitude band remains the primary driver; the growth rate increases with the increase of the strength of the high-latitude band.

By the time the low-latitude band is close to the equator (at 5°), the shrinking of the unstable domain in the parameter space of the high- and low-latitude bands' field strength can be seen. A stable (white regions) or only weakly unstable (darker-colored contours) domain can also be seen. This is very much like the features found in Figure 5 for the low G case. Both the antisymmetric and symmetric modes are not excited if there is no high-latitude band.

Next, let us investigate how the properties of band system migration change if the band is wider than 10° in latitude. Active regions often, particularly *nests*, indicate a wider latitudinal width of the toroidal band from which they originate. By performing a simulation of double-band MHD instability for a band pair of 15° latitudinal width each, we describe our results. Figure 7 reveals similar features of the instability of a double-band system with a width of 15° each. Although, in this case, it can also be clearly seen that the high-latitude band is the primary driver of the instability. However, due to the increased width of the band, the low-latitude band gains substantial importance in the MHD model. The symmetric and antisymmetric modes show similar features, again, with the high- and low-latitude bands at 60° and 30° latitudes. The biggest noticeable difference is that the lighter region i.e., the maximum

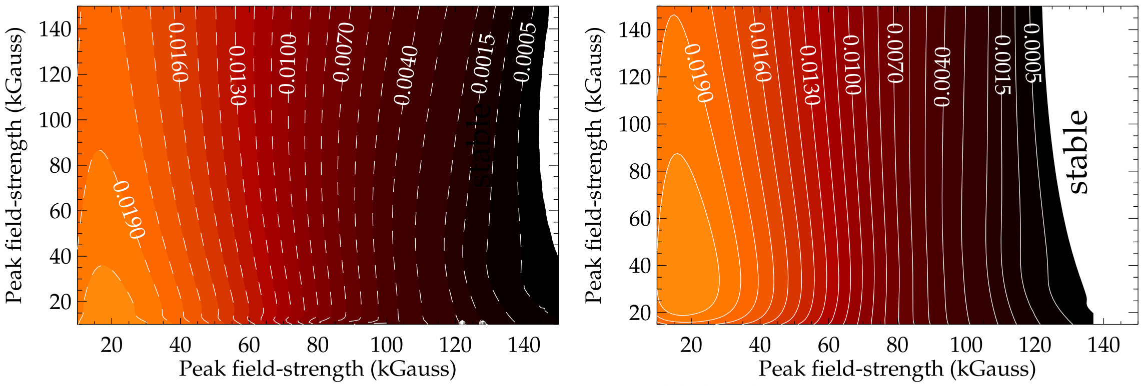
(aa) bands at 60° and 30°; G=0.5; m=1,A (ab) bands at 60° and 30°; G=0.5; m=1,S

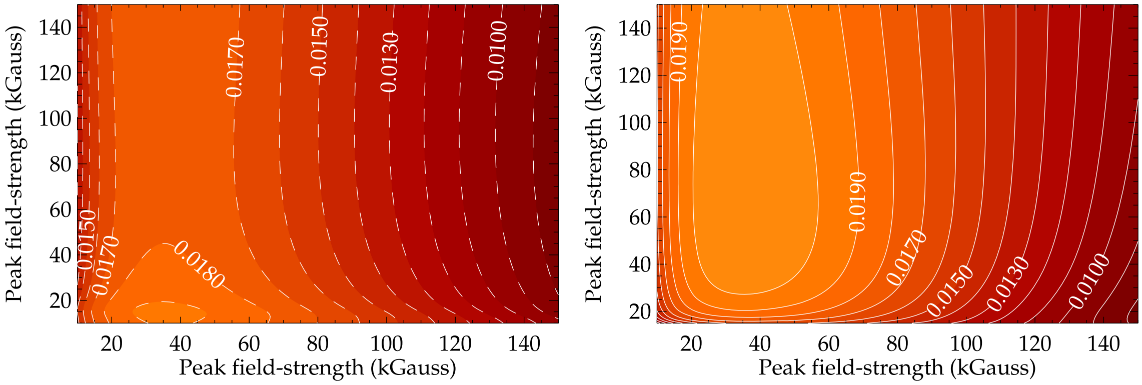
(ba) bands at 50° and 20°; G=0.5; m=1,A (bb) bands at 50° and 20°; G=0.5; m=1,S

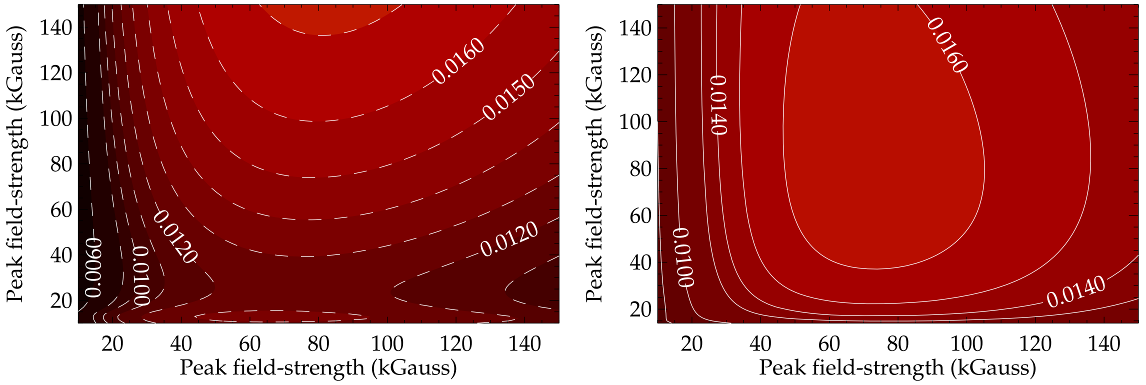
(ca) bands at 40° and 10°; G=0.5; m=1,A (cb) bands at 40° and 10°; G=0.5; m=1,S

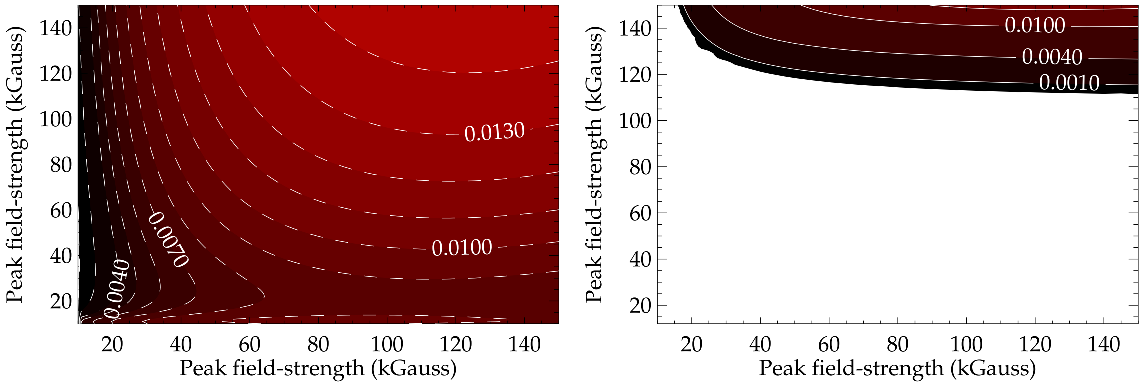
(da) bands at 35° and 5°; G=0.5; m=1,A (db) bands at 35° and 5°; G=0.5; m=1,S

Figure 7. For the $G = 0.5$ growth rate contours. The same as in Figure 5, but for bandwidth 15°.

unstable zone, which was vertical when the bandwidth was considered to be 10°, and also was almost independent of the low-latitude band strength, is now limited to a very small area on the graph when the peak field strength of the low-latitude band is about 10–20 kG, indicating the shrinkage of the unstable zone.

We can see that the low-latitude band starts taking on a relatively bigger role compared to the 10° band system in driving the instability, as this wider band system migrates toward 50° and at 20° latitude.

Panels (ca), (cb) and (da), (db) show an obvious difference between the two bandwidth values because the instabilities remain significantly stronger in the case of wider bands even at lower latitudes. Since the larger width favors the interaction between the bands, by contributing to making them in relatively closer proximity compared to the band system with 10° width.

In the radiative tachocline (Figure 8) when comparing panel (aa) with panel (ab), we do not find as much of a difference between the asymmetric and symmetric modes as we found in the case of narrow bands.

However, as the band system moves toward the equator, the differences between the two modes become evident. For antisymmetric modes, we notice that both the high- and low-latitude bands participate in driving the instability, and the highest growth rates occur at the location shown in the top right corner, i.e., for strong magnetic fields for both bands in the double-band system, in panels (bb)–(db) in the right column. On the other hand, for the symmetric modes, as the wider band system migrates toward the equator, it essentially becomes stable (see the blank region in the bottom right panels of Figures 7 and 8); the instability does not become excited until the high-latitude band reaches a strength of about 120 kG. Interestingly, one may note that the instability of the high-latitude band is not excited unless there is the presence of a low-latitude band with a moderate strength of about 25 kG.

In general, in both cases of 10° and 15° bandwidths, stability for the band system of the $m = 1$ symmetric mode increases when it becomes closer to the equator, as revealed from the extended blank regions in the bottom right panels of Figures 5–8. In Figures 5–8, the bottom left panels, which display the antisymmetric modes, all also show very weak instability. Essentially the band system becomes more stable when the low-latitude band (i.e., the active cycle's band) is nearing the end of that cycle.

3.3. Disturbance Patterns

When the high- and low-latitude bands in the double-band system are at 60° and 30° latitudes, we can see that the flows and the tachocline top-surface deformation are primarily confined within the two bands, indicating that the two bands are interacting between themselves (see the top two panels of Figures 9–10 (aa) and (ab)). The interaction between high- and low-latitude bands continues and increases as the band system moves toward the equator (i.e., the high- and low-latitude bands being at 50° and 20°, respectively). We can see in panels (ba) and (bb) that the flow vectors (white arrows) are again primarily confined between the two bands. The flow is geostrophic in all cases, i.e., the flow is clockwise in bulging (red-yellow color map) and counterclockwise in depression.

Interestingly, we do not see cross-hemispheric interaction via the flow vectors until the band system migrates further toward the equator. The low-latitude band starts cross-equatorial interactions with its opposite-hemisphere counterpart when it reaches below 15°. This can be seen in the bottom two rows. It is also clear that the low-latitude band acts as a barrier to the high-latitude band having a cross-hemispheric interaction. This barrier gets removed when there is an optimal distance of <30° between the low-latitude bands in the northern and southern hemispheres.

This is also the time when the solar cycle moves past its peak phase and enters its declining phase. This is evident from the latitude-longitude planes displayed in the bottom two rows, for the high- and low-latitude bands at 40° and 10° (panels (ca) and (cb)) and at 35° and 5° (panels (da) and (db)). So, here we see that the cross-equatorial communication between the active cycle's bands (the low-latitude bands in the north and south) starts after the active cycle has passed its peak. Recall the growth rate contours shown in Figure 5, we can note that the band system becomes either stable or weakly unstable when the low-latitude band is as close as 10° from the equator. The low-latitude band itself becomes inactive unless the field strength is very high, and it creates a barrier for the high-latitude band to become active.

The analyses of the results for the radiative tachocline give a very similar picture in many aspects. When the high- and low-latitude bands in the double-band system are at 60° and 30° latitudes, respectively, both bands are busy interacting with each other. This situation also continues for the two bands at 50° and 20° latitudes, respectively. However, when the two bands in the double-band system are at 40° and 10° latitudes, respectively, or lower than that, the low-latitude band stops interacting with the high-latitude band, and starts the cross-hemispheric communication via the flow vectors with its opposite-hemisphere counterpart.

In both G cases (i.e., for $G = 0.5$ and 100), it can be seen that the asymmetric modes vanish by the time the low-latitude band is as close as 5° from the equator. This is because the flow is antisymmetric about the equator for the antisymmetric modes, and there is no spatial domain for the flow to change sign to satisfy this particular symmetry condition. Therefore, the antisymmetric unstable modes disappear.

4. Physics of Cross-equatorial Interactions and Their Nonlinear Consequences

As we have mentioned in the previous sections, cross-equatorial interactions of the bands occur when they are close to the equator. The question is what could the physics of such an interaction be? We briefly described in the Introduction what to expect from the linear instability theory, such as that demonstrated in Figure 4 of Cally et al. (2003), namely, how the in-phase or antiphase tipping of a toroidal band can occur, respectively, for a symmetric or antisymmetric mode, the linear and ideal MHD models cannot really answer the question regarding the reality of cross-equatorial interaction of bands. To materialize the concept of cross-equatorial interaction, both nonlinearity and viscous/turbulent dissipation are needed.

Cross-equatorial interactions of the bands can form from antiphase tipping, i.e., from the antisymmetric mode of the instability. Nonlinear evolution can tell us how large an amplitude in latitude displacement a toroid can have in each hemisphere, and therefore how close the toroids in the northern and southern hemispheres can get to each other. This requires at least a quasi-3D thin-shell or a shallow-water model because it needs to reduce the mass remaining between the northern and southern bands. Some turbulent magnetic diffusion is also needed to complete the connection of the northern and southern bands.

When this occurs it is possible that some magnetic energy will be released due to slow reconnection at the longitude (aa) bands at 60° and 30°; G=100; m=1,A (ab) bands at 60° and 30°; G=100; m=1,S

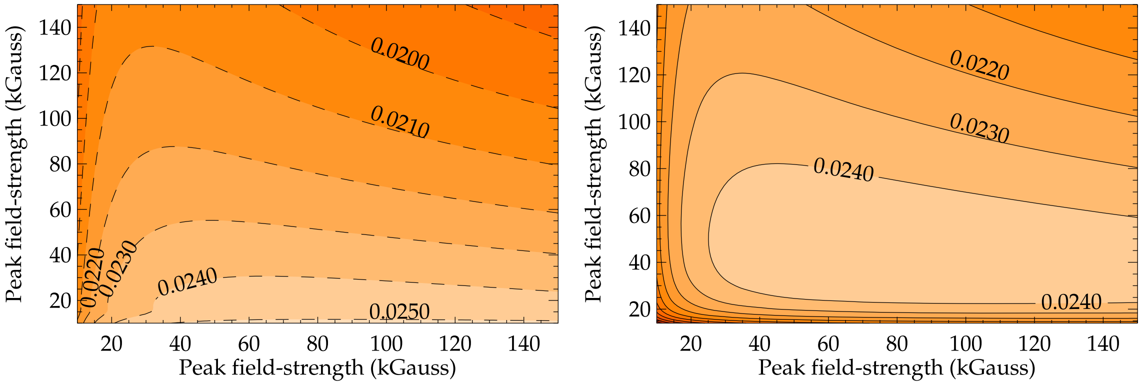

(ba) bands at 50° and 20°; G=100; m=1,A (bb) bands at 50

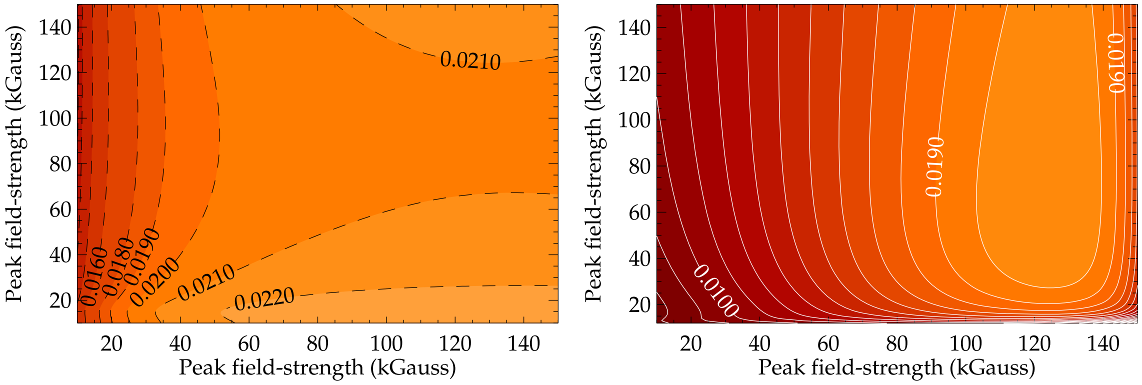

(ca) bands at 40° and 10°; G=100; m=1,A (cb) bands at 40° and 10°; G=100; m=1,S

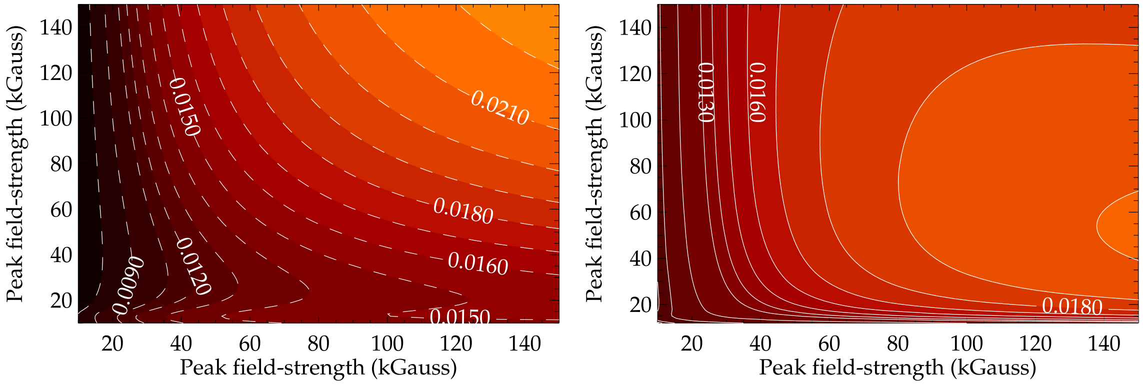

(da) bands at 35° and 5°; G=100; m=1,A (db) bands at 35° and 5°; G=100; m=1,S

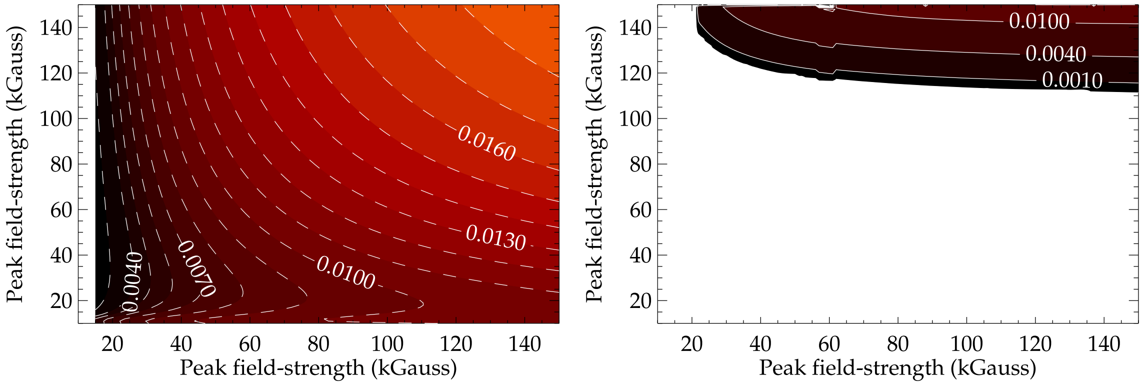

Figure 8. For the $G = 100$ growth rate contours. The same as in Figure 6, but for bandwidth 15°.

where the bands are coming in contact. As part of this process, it could become a site for the new emergence of magnetic flux. However, this reconnection would also lead to the annihilation of oppositely directed toroidal flux about the equator, which is expected to be locally relevant near the equatorial regions only. But this is not expected to have a large-scale immediate impact

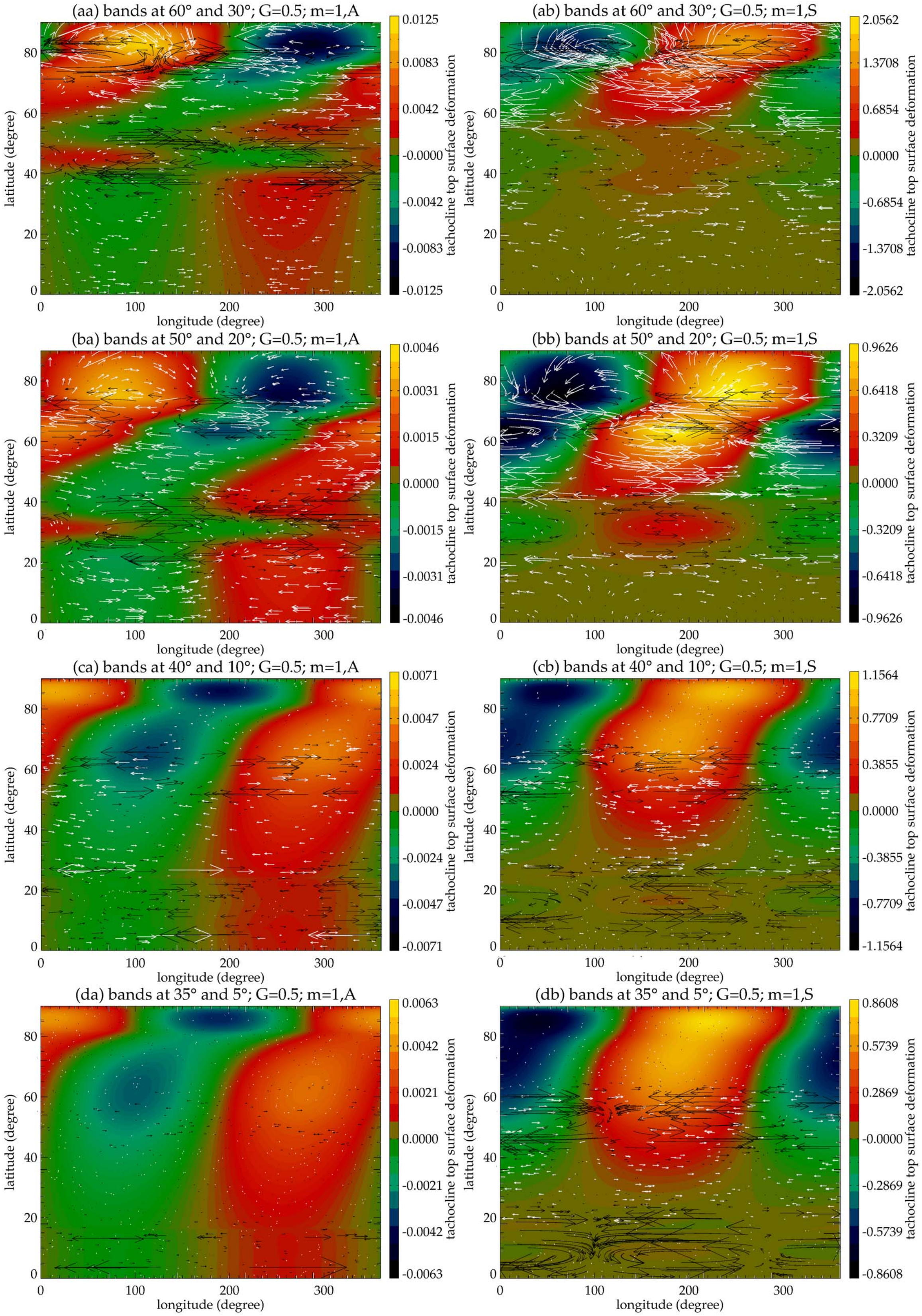

Figure 9. Snapshots of velocity and magnetic disturbance patterns are shown in the latitude-longitude plane for the symmetric and asymmetric $m = 1$ modes. Black arrows represent the magnetic field vector, white arrows flow vectors, and the color map the tachocline top surface deformation (red-yellow denotes the bulging of the top surface, and green-blue the depression). This figure shows the eigenfunctions for the overshoot part of the tachocline ($G = 0.5$).

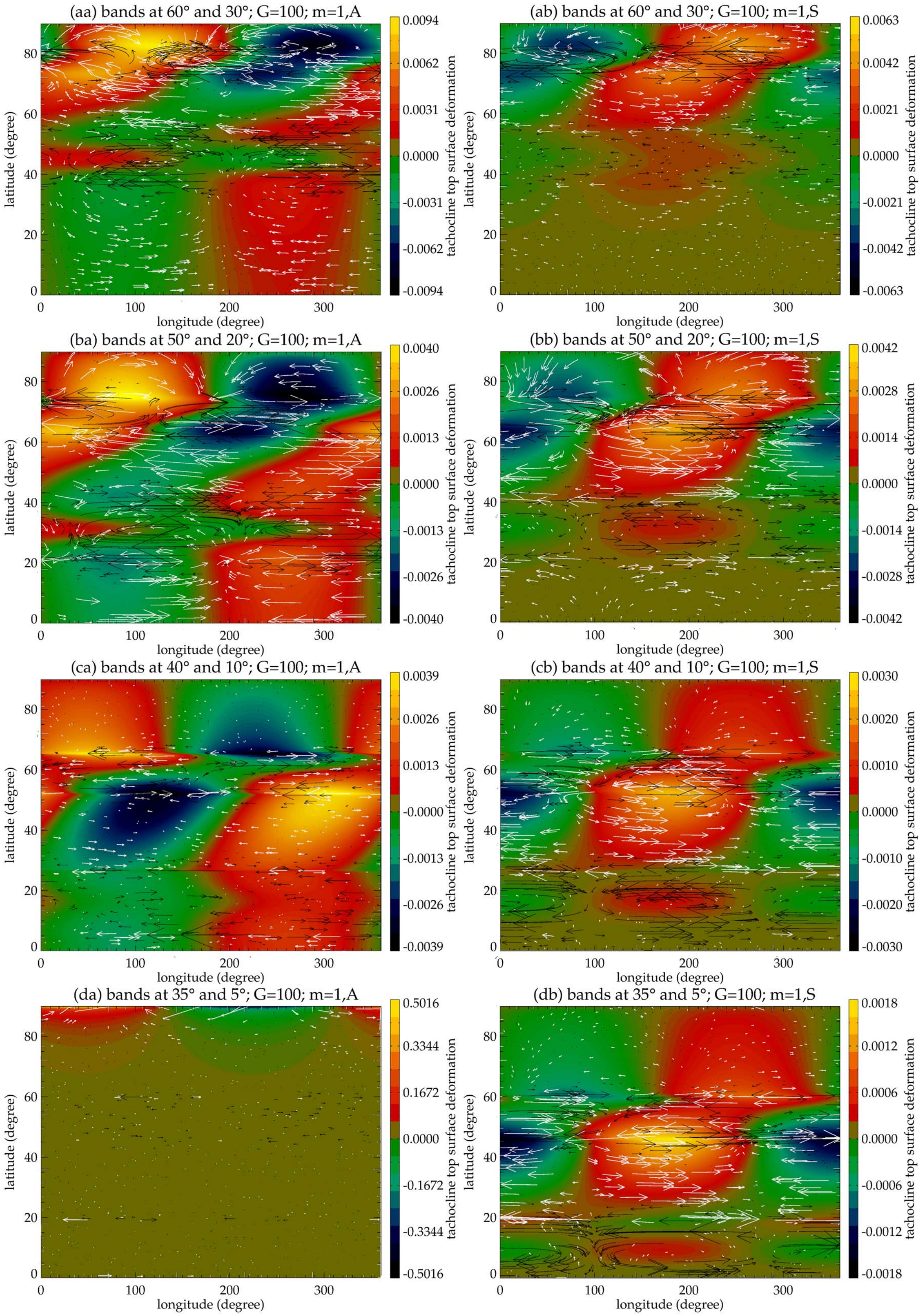

Figure 10. The same as Figure 9, but for the radiative part of the tachocline ($G = 100$).

in a high beta plasma where the cross-equatorial cancellation is primarily being driven by a slow counterflow or turbulent dissipation. So the question is, how long may it take to have a cross-equatorial interaction between the bands in the northern and southern hemispheres when they are in close proximity at certain longitudes due to antiphase tipping? If we suppose that the bands have come so close to each other at a certain longitude that their separation is just 1°, then essentially the two bands are physically separated by the distance $L = (\pi/180) \times 5 \times 10^{10}$ cm at the tachocline region. If the turbulent diffusivity η is $3 \times 10^{11}\,\mathrm{cm^2\,s^{-1}}$, the diffusion time would be L^2/η, which comes out to be approximately 1 month, for the bands to start their cross-equatorial interaction. Therefore, we can conceptually understand the physics and an approximate timescale of the cross-equatorial interaction. However, quantitative estimates of this interaction and its consequences on solar magnetism observed at the surface are beyond the scope of this paper. A forthcoming paper with the inclusion of turbulent diffusivity and nonlinear evolution can address this issue in more detail. Nonetheless, the consequences of such interactions have been discussed in McIntosh & Leamon (2014).

If the symmetric mode is the dominant mode, the tipping of the bands in the northern and southern hemispheres would take place in phase. For in-phase tipping, the bands will not be able to do cross-equatorial interactions by diffusion at any longitude, instead, they would maintain a uniform latitude separation between them throughout the longitude. However, in this case, either a portion of the band in the northern hemisphere can cross the equator and move to the band in the southern hemisphere, or vice versa. As one of the plausible consequences of this in-phase tipping, bands can lead to the emergence of anti-Hale spots, particularly when they are close to the equator. In this case, the spots that manifest as anti-Hale spots may essentially be appearing from the tipped portion of the band in the opposite hemisphere at a certain longitude.

5. Concluding Remarks

We explore here the MHD instability of a double-band system with the latitudinal separation of 30° between the high- and low-latitude bands. We present our main conclusions below.

1. We find that the double-band system is unstable to $m = 1$ and 2 modes with both symmetries about the equator, namely the symmetric and antisymmetric modes. $m = 1$ modes are unstable for a wider range of field strengths than the $m = 2$ modes.
2. As found in the single-band case, the $m = 1$ modes reach an asymptotic value of growth rate as the field strength is increased in the case of a high $G = 100$, the double-band system shows this feature too. However, there is a cutoff in the instability for these modes when the G value is low.
3. As the double-band system migrates toward the equator, we find that the high- and low-latitude bands interact in the same hemisphere when they are at 60° and 30° latitudes.
4. Their interactions continue as they migrate toward the equator, namely, when they are at 50° and 20° latitudes.
5. When the band system migrates further toward the equator, namely when they are at 40° and 10° latitudes, respectively, the low-latitude band stops interacting with the high-latitude bands and starts cross-hemispheric interaction with its opposite-hemisphere counterpart. This is also the time when the active cycle passes the peak phase and is in its declining phase.
6. When the interaction between the high- and low-latitude band stops in each hemisphere, and cross-hemispheric communication starts, the band system becomes either stable for a wide range of field strengths of the low-latitude band (i.e., the active cycle's band) or only weakly unstable for a very high field strength of the low-latitude band (>60 kG or so).
7. Since the high-latitude band is the primary driver of the instability of the double-band system, this instability starts weakening, eventually resulting in disappearance when the low-latitude band does not interact with the high-latitude band, and starts the cross-equatorial interaction with its opposite-hemisphere counterpart. We see that this happens during the declining phase of the active cycle.
8. Finally, we explained conceptually the physics of how the cross-equatorial interaction can occur when the bands in the northern and southern hemispheres are in close proximity at certain longitudes. However, to explore the details of this interaction, turbulent diffusivity and nonlinear evolution need to be included in the shallow-water model.

There is much observational evidence of an extended solar cycle, or equivalently, overlapping cycles. While zones of sunspots rarely overlap between adjacent cycles, other magnetic activity measures of a new cycle beginning at high latitudes usually overlap in time with low-latitude activity. If the toroidal bands, responsible for emerging spots and the other activity signals at higher latitudes reside in the solar tachocline, or at the bottom half of the convection zone. It is worth examining the differences in the global MHD of the tachocline between when a single toroidal band is present at sunspot latitudes, and when there is a second band, of opposite polarity, at much higher latitudes. We have presented our results of the study performed here for a double-band system separated in latitude by 30°. But this latitude separation between the bands can be smaller or larger than 30°. A forthcoming paper will report a study of how the instability features change when the high- and low-latitude bands are separated by 25° or 35°.

The bandwidth has been fixed at 10° latitudinal width for each band in this study. While the 10° width of the spot-producing toroidal band is a reasonable choice, other bandwidths, such as narrower or broader than 10° can be studied in the future.

This work is supported by Newton International Fellowship of The Royal Society, program No. NIF-R1-192417. This research was supported by the Hungarian Science Research Fund (OTKA grant Nos. 128221 and K-142987). This work is also supported by the National Center for Atmospheric Research, which is a major facility sponsored by the National Science Foundation under cooperative agreement 1852977. M. D. acknowledges partial support from various NASA grants, such as NASA-LWS award 80NSSC20K0355 (awarded to NCAR), NASA-HSR award 80NSSC21K1676 (awarded to NCAR), and NASA-DRIVE Center award 80NSSC20K0602 (awarded to Stanford).

Appendix A
Nonlinear MHD Shallow-water Equations

The MHD equations are presented in a rotating frame of reference (rotating with core rotation ω_c, which is equal to the rotation rate at 32° at tachocline depth). We define the velocity as $\boldsymbol{V} = u\hat{\lambda} + v\hat{\phi}$ and the magnetic field as $\boldsymbol{B} = a\hat{\lambda} + b\hat{\phi}$, where $\hat{\lambda}$ and $\hat{\phi}$ are unit vectors in the longitudinal and latitudinal directions, respectively. The horizontal components of both the flow and the magnetic fields are independent of height, while the radial components (w and c) are linear functions of height. The fluid moves horizontally in compressible and expanding vertical columns according to mass conservation, as it appears as the movement of a deformable surface (Dikpati et al. 2018). Because the tachocline has a large shear as the rotation rate changes rapidly, large-scale magnetic fields can be formed. These fields are conserved in the layer and the magnetic field lines remain at the top of the surface.

The total pressure gradient, the sum of hydrostatic and magnetic gradients, is proportional to the horizontal gradient of thickness. Shallow-water systems usually include no diffusion and so they represent *ideal fluids*. The total energy is conserved, including kinetic, potential, and magnetic energies. The nonlinear one-layer, dimensionless MHD shallow-water equations are written as

$$\begin{aligned}\frac{\partial u}{\partial t} = {} & \frac{v}{\cos\phi}\left[\frac{\partial v}{\partial\lambda} - \frac{\partial}{\partial\phi}(u\cos\phi)\right] \\ & - \frac{1}{\cos\phi}\frac{\partial}{\partial\lambda}\left(\frac{u^2+v^2}{2}\right) - G\frac{1}{\cos\phi}\frac{\partial h}{\partial\lambda} + 2\omega_c v\sin\phi \\ & - \frac{b}{\cos\phi}\left[\frac{\partial b}{\partial\lambda} - \frac{\partial}{\partial\phi}(a\cos\phi)\right] + \frac{1}{cos\phi}\frac{\partial}{\partial\lambda}\left(\frac{a^2+b^2}{2}\right)\end{aligned} \tag{A1}$$

$$\begin{aligned}\frac{\partial v}{\partial t} = {} & -\frac{u}{\cos\phi}\left[\frac{\partial v}{\partial\lambda} - \frac{\partial}{\partial\phi}(u\cos\phi)\right] \\ & - \frac{\partial}{\partial\phi}\left(\frac{u^2+v^2}{2}\right) - G\frac{\partial h}{\partial\phi} + 2\omega_c u\sin\phi \\ & + \frac{a}{\cos\phi}\left[\frac{\partial b}{\partial\lambda} - \frac{\partial}{\partial\phi}(a\cos\phi)\right] + \frac{\partial}{\partial\phi}\left(\frac{a^2+b^2}{2}\right),\end{aligned} \tag{A2}$$

$$\begin{aligned}\frac{\partial}{\partial t}(1+h) = {} & -\frac{1}{\cos\phi}\frac{\partial}{\partial\lambda}((1+h)u) \\ & - \frac{1}{\cos\phi}\frac{\partial}{\partial\phi}((1+h)v\cos\phi),\end{aligned} \tag{A3}$$

$$\begin{aligned}\frac{\partial a}{\partial t} = {} & \frac{\partial}{\partial\phi}(ub - va) + \frac{a}{\cos\phi}\left(\frac{\partial u}{\partial\lambda} + \frac{\partial}{\partial\phi}(v\cos\phi)\right) \\ & - \frac{u}{\cos\phi}\left(\frac{\partial a}{\partial\lambda} + \frac{\partial}{\partial\phi}(b\cos\phi)\right),\end{aligned} \tag{A4}$$

$$\begin{aligned}\frac{\partial b}{\partial t} = {} & -\frac{1}{\cos\phi}\frac{\partial}{\partial\lambda}(ub - va) + \frac{b}{\cos\phi}\left(\frac{\partial u}{\partial\lambda} + \frac{\partial}{\partial\phi}(v\cos\phi)\right) \\ & - \frac{v}{\cos\phi}\left(\frac{\partial a}{\partial\lambda} + \frac{\partial}{\partial\phi}(b\cos\phi)\right),\end{aligned} \tag{A5}$$

$$\frac{\partial}{\partial\lambda}((1+h)a) + \frac{\partial}{\partial\phi}((1+h)b\cos\phi) = 0. \tag{A6}$$

The radius (r_0) of the shell and inverse of the interior rotation rate (ω_c) are determined as the length and timescale. $G = gH/r_0^2\omega_c^2$ is a dimensionless measure of the reduced gravity of the stratified tachocline and g is the reduced gravity of the stratified layer of undisturbed dimensional thickness H (see Gilman 2000 for more details). G can be related to the fractional departure of the actual temperature gradient from the adiabatic gradient: $G \sim 10^3|\nabla - \nabla_{\mathrm{ad}}|$. For the overshoot layer of the tachocline (located between 0.7 and 0.72 $R_\odot$), the value of *dimensionless reduced gravity* is $10^{-2} \lesssim G \lesssim 10^{-1}$, and in the radiative tachocline (located between 0.68 and 0.7 $R_\odot$) it is $10^1 \lesssim G \lesssim 10^2$.

The latitudinal differential rotation, as derived from helioseismology, can be expressed in the rotating frame as

$$\omega_0 = s_0 - s_2\mu^2 - s_4\mu^4 - \omega_c, \tag{A7}$$

where μ is the sine latitude and s_0, s_2, and s_4 are coefficients. The interior rotation rate, (ω_c), approximately matches the rotation rate at 32° latitude at the tachocline. The s_0 parameter is the rotation rate at the equator and the differential rotation amplitude becomes $(s_2 + s_4)/s_0$ (Dikpati et al. 2018).

Appendix B
Linearized Perturbation Equations

For completeness, we present a short description of the linearized perturbation equations. Splitting the velocity and the magnetic field components into reference state (longitude-averaged) and perturbation quantities, we write $u = u_0 + u'$, $\mathrm{v} = \mathrm{v}'$, $a = a_0 + a'$, and $b = b'$, where 0 denotes the reference state and primes denote the perturbation. Then the zeroth-order and first-order perturbation equations can be obtained by linearizing the nonlinear governing equations. The zeroth-order equation gives us a relation between the reference state pressure, velocity, and magnetic field. The first-order perturbation equations define the time evolution of the disturbances. Since the perturbations are two dimensional, they can be expressed as stream functions to satisfy the continuity equations and thus can be written as follows:

$$\begin{aligned}u' &= -\frac{\partial\psi}{\partial\phi}, \\ v' &= \frac{1}{\cos\phi}\frac{\partial\psi}{\partial\lambda}, \\ a' &= -\frac{\partial\chi}{\partial\phi}, \\ b' &= \frac{1}{\cos\phi}\frac{\partial\chi}{\partial\lambda},\end{aligned} \tag{B1}$$

where ψ represents the velocity stream function and χ the corresponding magnetic field stream function. ψ and χ can be transformed with respect to longitude (λ) and time (t). We assume all perturbations are $\sim e^{im(\lambda - ct)}$, where m is the longitudinal wavenumber. $c = c_r + ic_i$ gives both the angular speed in the longitude and phase speed c_r of the perturbation, which is complex for growing or decaying modes and real for neutral modes and its growth rate mc_i. The perturbation Equations (A1)–(A6) concern the reference state differential rotation u_0, toroidal field a_0, and shell thickness $(1 + h_0)$, replacing the latitude ϕ by $\mu = \sin\phi$ and introducing angular measures

$$a_0 = \alpha_0(1 - \mu^2)^{1/2}, \tag{B2}$$

$$u_0 = \omega_0(1-\mu^2)^{1/2}. \tag{B3}$$

The height (h_0) of the reference state fluid is determined by

$$G\frac{\partial h_0}{\partial \phi} = -u_0^2 \tan\phi. \tag{B4}$$

Then the resulting $m \neq 0$ first-order perturbation equations are given by

$$\begin{aligned} im(\omega_0 - v)u + c\frac{d}{d\mu}[(1-\mu^2)\omega_0] = -\frac{imG}{(1-\mu^2)^{1/2}}h \\ + im\alpha_0 a + b\frac{d}{d\mu}[(1-\mu^2)\alpha_0], \end{aligned} \tag{B5}$$

$$\begin{aligned} im(\omega_0 - c)v + 2\omega_0\mu u = -(1-\mu^2)^{1/2}G\frac{dh}{d\mu} \\ + 2\alpha_0\mu a + im\alpha_0 b, \end{aligned} \tag{B6}$$

$$\begin{aligned} im(\omega_0 - c)h + \frac{(1+h_0)}{(1-\mu^2)^{1/2}}imu \\ + \frac{d}{d\mu}[(1+h_0)(1-\mu^2)^{1/2}v] = 0, \end{aligned} \tag{B7}$$

$$\begin{aligned} & im(\omega_0 - c)a - \alpha_0\left\{imu + (1-\mu^2)^{1/2}\frac{d}{d\mu}[(1-\mu^2)^{1/2}v]\right\} \\ & + \omega_0(1-\mu^2)^{1/2}\frac{d}{d\mu}[(1-\mu^2)^{1/2}b] \\ & - (1-\mu^2)^{1/2}\frac{d}{d\mu}[(1-\mu^2)^{1/2}(\omega_0 b - \alpha_0 v)] = 0, \end{aligned} \tag{B8}$$

$$im(\omega_0 - c)b - im\alpha_0 v = 0, \tag{B9}$$

$$\begin{aligned} & im(1-\mu^2)^{1/2}\alpha_0 h + im(1+h_0)a + (1-\mu^2)^{1/2} \\ & \times \frac{d}{d\mu}[(1+h_0)(1-\mu^2)^{1/2}b] = 0. \end{aligned} \tag{B10}$$

To solve Equations (B5)–(B10), it is convenient to further reduce the system to two equations, in v and h. This system can be solved as it is even in the limit of a zero toroidal field, or $\alpha_0 \to 0$, as well as the limit of $G \to \infty$, which is effectively the two-dimensional limit. The two remaining equations are

$$\begin{aligned} & (1-\mu^2)^{3/2}S_r S_m(1+h_0)\frac{dv}{d\mu} + (1-\mu^2)^{1/2} \\ & \times \left((1-\mu^2)S_r S_m\frac{dh_0}{d\mu} - S_r S_m(1+h_0)\mu - S_m\right. \\ & \times \left.\left\{\frac{d}{d\mu}[\omega_0(1-\mu^2)]\right\}(1+h_0)\right)v + imS_r^2 S_g h = 0, \end{aligned} \tag{B11}$$

$$\begin{aligned} & m(1-\mu^2)^{1/2}S_r^2 G(1+h_0)\frac{dh}{d\mu} + 2m(1-\mu^2)^{1/2}S_r^2 \\ & \times (\alpha_0^2 - S_r\omega_0)h - 2i\mu(1-\mu^2)(\alpha_0^2 - S_r\omega_0)(1+h_0)\frac{dv}{d\mu} \\ & - i\left[2\mu(1-\mu^2)S_r(\alpha_0^2 - S_r\omega_0)\frac{dh_0}{d\mu}\right. \\ & - 2\mu(1+h_0)S_r(\alpha_0^2 - S_r\omega_0) \\ & - m^2 S_r S_m(1+h_0) + 2\alpha_0\mu(1-\mu^2) \\ & \times \left.\left(S_r\frac{d\alpha_0}{d\mu} - \alpha_0\frac{d\omega_0}{d\mu}\right)(1+h_0)\right]v \ = \ 0, \end{aligned} \tag{B12}$$

where

$$\begin{aligned} & S_r = \omega_0 - c, \\ & S_m = (\omega_0 - c)^2 - \alpha_0^2, \\ & S_g = (1-\mu^2)[(\omega_0 - c)^2 - \alpha_0^2] - G(1+h_0). \end{aligned} \tag{B13}$$

Appendix C
Solution Method

For α_0 antisymmetric and ω_0 symmetric, we have two possible symmetries for the perturbation variables: (1) if v, a are symmetric and u, b, h are antisymmetric about $\mu = 0$, we refer to it as a *symmetric mode*, and (2) if v, a are antisymmetric and u, b, h are symmetric about $\mu = 0$, we refer to it as an *antisymmetric mode*. To avoid any nonphysical behavior at the poles, ψ and χ are omitted at the poles. The shooting method is described in in detail in Press et al. (1992).

ORCID iDs

Bernadett Belucz https://orcid.org/0000-0002-0040-1790
Mausumi Dikpati https://orcid.org/0000-0002-2227-0488
Scott W. McIntosh https://orcid.org/0000-0002-7369-1776
Robert J. Leamon https://orcid.org/0000-0002-6811-5862
Robertus Erdélyi https://orcid.org/0000-0003-3439-4127

References

Brown, T. M., Christensen-Dalsgaard, J., Dziembowski, W. A., et al. 1989, ApJ, 343, 526
Cally, P. S. 2001, SoPh, 199, 231
Cally, P. S., Dikpati, M., & Gilman, P. A. 2003, ApJ, 582, 1190
Chatterjee, S., Banerjee, D., McIntosh, S. W., et al. 2019, ApJL, 874, L4
Cliver, E. W. 2014, SSRv, 186, 169
Dikpati, M., Belucz, B., Gilman, P. A., et al. 2018, ApJ, 862, 159
Dikpati, M., Cally, P. S., McIntosh, S. W., & Heifetz, E. 2017, NatSR, 7, 14750
Dikpati, M., & Gilman, P. A. 1999, ApJ, 512, 417
Dikpati, M., & Gilman, P. A. 2001a, ApJ, 551, 536
Dikpati, M., & Gilman, P. A. 2005, ApJL, 635, L193
Dikpati, M., Gilman, P. A., & Rempel, M. 2003, ApJ, 596, 680
Dikpati, M., McIntosh, S. W., Bothun, G., et al. 2018, ApJ, 853, 144
Dikpati, M., McIntosh, S. W., Chatterjee, S., et al. 2019, NatSR, 9, 2035
Dikpati, M., McIntosh, S. W., & Wing, S. 2021, FrASS, 8, 71
Galloway, D. J., & Weiss, N. O. 1981, ApJ, 243, 945
Gilman, P. A. 2000, ApJL, 544, L79
Gilman, P. A., & Dikpati, M. 2000, ApJ, 528, 552
Gilman, P. A., & Dikpati, M. 2002, ApJ, 576, 1031
Gilman, P. A., & Fox, P. A. 1997, ApJ, 484, 439
Goode, P. R., Dziembowski, W. A., Korzennik, S. G., et al. 1991, ApJ, 367, 649

Guerrero, G., & Käpylä, P. J. 2011, A&A, 533, A40
Guerrero, G., Smolarkiewicz, P. K., de Gouveia Dal Pino, E. M., Kosovichev, A. G., & Mansour, N. N. 2016, ApJL, 828, L3
Howe, R., Hill, F., Komm, R., et al. 2011, JPhCS, 271, 012074
Harvey, K. L., & Martin, S. F. 1973, SoPh, 32, 389
Lau, K. M., & Peng, L. 1987, JAtS, 44, 950
Martin, S. F. 2018, FrASS, 5, 17
McIntosh, S. W., Wang, X., Leamon, R. J., et al. 2014a, ApJ, 792, 12
McIntosh, S. W., Wang, X., Leamon, R. J., et al. 2014b, ApJL, 784, L32
McIntosh, S. W., & Leamon, R. J. 2014, ApJL, 796, 6
McIntosh, S. W., Leamon, R. J., Krista, L. D., et al. 2015, NatCo, 6, 6491
Muñoz-Jaramillo, A., Nandy, D., & Martens, P. C. H. 2009, ApJ, 698, 461
Nandy, D., & Choudhuri, A. R. 2002, Sci, 296, 1671
Osborne, A. R., Segre, E., Boffetta, G., & Cavaleri, L. 1991, PhRvL, 67, 592
Parker, E. N. 1955, ApJ, 121, 491
Parker, E. N. 1975, ApJ, 198, 205
Press, W. H., Teukolsky, S. A., Vetterling, W. T., & Flannery, B. P. 1992, Numerical Recipes in Fortran. (2nd edn.; Cambridge: Cambridge Univ. Press)
Pipin, V. V., & Kosovichev, A. G. 2020, ApJ, 900, 11
Schecter, D. A., Boyd, J. F., & Gilman, P. A. 2001, ApJL, 551, L185
Snodgrass, H. B. 1987, SoPh, 110, 35
Tappin, S. J., & Altrock, R. C. 2013, SoPh, 282, 249
Tomczyk, S., Schou, J., & Thompson, M. J. 1995, ApJ, 448, 57
Weber, M., Fan, Y., & Miesch, M. S. 2011, ApJ, 741, 14
Wilson, P. R., Altrocki, R. C., Harvey, K. L., Martin, S. F., & Snodgrass, H. B. 1988, Natur, 333, 748
Zaqarashvili, T. V. 2018, ApJ, 856, 32
Zaqarashvili, T. V., Carbonell, M., Oliver, R., et al. 2010, ApJ, 709, 749
Zaqarashvili, T. V., Oliver, R., & Ballester, J. L. 2009, ApJL, 691, L41